

MOF Derived Ni-Cu Double Hydroxide Based Self-Powered Flexible Asymmetric Supercapacitor Using Onion Scale as an Effective Bio-Piezoelectric Separator

Parna Maity,^[a] Anirban Maitra,^[a] Suparna Ojha,^[a] Ankita Mondal,^[a] Aswini Bera,^[a] Sumanta Bera,^[a] Arkapriya Das,^[a] and Bhanu Bhushan Khatua^{*[a]}

Modern electronic devices necessitate the utilization of compact, wearable, and flexible substrates capable of simultaneously harvesting and storing energy by merging traditional energy harvesting techniques with storage mechanisms into a singular portable device. Here, we present the fabrication of a low-cost, sustainable, all-solid-state, self-powered flexible asymmetric supercapacitor (SPASC) device. This device features MOF-derived nickel-copper double hydroxide nanosheets coated stainless steel (SS) fabric sheet (NCDH@SS) as the positive electrode, while manganese dioxide decorated activated porous carbon on SS fabric sheet (MnO_2 -APC@SS) acts as the negative electrode. The electrodes are isolated by a PVA-KOH gel electrolyte, while onion scale, a bio-piezoelectric separator,

ensures effective separation. The self-charging ability of the device is demonstrated through mechanical deformation induced by finger imparting. This rectification-free SPASC device exhibits remarkable performance, achieving a charge up to ~ 235.41 mV from the preliminary open circuit voltage of ~ 20.89 mV within 180 s under ~ 16.25 N of applied compressive force (charged up to ~ 214.52 mV). Furthermore, three SPASC devices connected in series can power up various portable electronic devices like wristwatches, calculators, and LEDs upon frequent imparting. Our work thus demonstrates an innovative and advanced approach towards the development of sustainable, flexible, and advanced self-powered electronics.

1. Introduction

In recent decades, the rapidly evolving global economy has led to a swift depletion of fossil fuels. Thus, an efficient conversion and storage of ambient energy is required to meet the demands of current technology and energy issues. To address these challenges, researchers are increasingly focusing on designing and fabricating efficient devices with energy conversion and storing capabilities for harnessing sustainable, renewable, and clean energies.^[1] Typically, harvesting and storing energy represent two separate domains within renewable energy, each often addressed independently through the use of distinct devices. The combination of these two distinct phenomena culminates in a continuous, small-scale self-charging power system.^[2–6] Mechanical-to-electrical and electrical-to-electrochemical energy conversion are two distinct mechanisms that can lead to simultaneous energy conversion and storage, leading to self-charging.^[7] Nanogenerators (NGs) are considered as one of the best choices for ambient energy conversion, whereas supercapacitors (SCs) or batteries are extensively used for energy storage.^[8–11] Piezoelectric and triboelectric nanogenerators are commonly utilized to promptly harvest electrical

energy from external mechanical forces. Generally, poly(vinylidene fluoride) (PVDF),^[12,13] poly(vinylidene fluoride-co-hexafluoropropylene) (PVDF-HFP),^[14] poly(L-lactic acid) (PLLA),^[15] poly(vinylidene fluoride-trifluoroethylene) (PVDF-TrFE)^[16] etc. polymers are utilized for harvesting the piezoelectric energy. In other ways, supercapacitors or ultracapacitors stand out as a convenient candidate for energy storage, owing to their rapid charge-discharge capabilities with elevated power density and prolonged cyclic stability.^[8,17,18] Usually, carbonaceous materials like activated carbon, carbon nanotube (CNT), and porous graphene are often used as electrode materials for electrical double layer type electrodes.^[19–22] On the other hand, an array of simple, binary and ternary transition metal-based oxides, sulfides, and hydroxides are used as suitable materials for pseudocapacitive electrodes.^[23–29] Depending upon the fabrication of the device, generally two types of supercapacitors are available: one is the symmetric supercapacitor with two similar electrodes that operate within a relatively narrow potential range,^[30,31] and the other one is the asymmetric supercapacitor device with a broad potential range and composed of two distinct electrode materials.^[32,33]

Numerous significant problems have arisen during the integration of two of these energy-related technologies regarding the size and weight of the devices, along with the complexity of their operating mechanisms. On the other hand, a rectifier-based electronic circuit is further important for converting the AC signal obtained from the external mechanical energy into electrochemical energy (DC signal) for storage purposes.^[34] During this conversion process, there is an unavoidable enhancement in the internal resistance combined

[a] P. Maity, A. Maitra, S. Ojha, A. Mondal, A. Bera, S. Bera, A. Das, B. Bhushan Khatua
Materials Science Centre, Indian Institute of Technology, Kharagpur 721302, India
Tel.: +91-3222-283982
E-mail: khatuabb@matsc.iitkgp.ac.in

 Supporting information for this article is available on the WWW under <https://doi.org/10.1002/batt.202400369>

with a simultaneous decrease in the integration density of the power-supplying devices, leading to unnecessary energy loss.^[35,36] To solve this problem, researchers have dedicated their efforts to achieve the direct transformation of electrochemical energy from mechanical energy in a one-step process, avoiding the need for rectification.^[35,37] A ‘piezoelectric driven self-charging supercapacitor power cell’ is demonstrated by Ramadoss *et al.* that follows a fascinating mechanism for directly transforming mechanical energy to electrochemical energy. This was achieved using a PVDF-ZnO film which, in addition to a piezoelectric material, acts as the separator between two supercapacitor electrodes. Under repeated palm impact within 300 s, the SCSPC device was charged up to ~110 mV from the initial open circuit potential (V_{oc}).^[38] Mitra *et al.* fabricated a rectification-free, wearable, and biocompatible SCASC device integrated with a fish bladder, that was utilized as a bio-piezoelectric separator. With continuous human finger pressure, their fabricated device was charged up to ~281 mV from the primary V_{oc} of ~130 mV.^[8] Song *et al.* also reported a rectification free piezo-supercapacitor featuring a PVDF-based separator and electrodes with functionalized carbon cloths. Under continuous compressive force at 4.5 Hz of frequency, the device was charged up to a maximum of 100 mV within 40 s.^[35] A self-charging supercapacitor was designed by Zhao *et al.* using multiscale polyacrylonitrile fiber as the piezoelectric separator.^[39] On application of a 30 N force at 1.5 Hz frequency, the device was charged up to 117 mV. Gao *et al.* fabricated a solid-state self-charging supercapacitor power cell composed of P(VDF-TrFE)/BTO piezo-film, NiCoP/NiCoN as the positive electrode, and Ac as the negative electrode and the device was charged to 132 mV in 155 s.^[40]

Research on piezo-supercapacitor devices indicates that the principal factor enhancing electrolyte ions transfer rate toward the supercapacitor electrodes is the electrostatic potential generated during the compression of the piezoelectric film, where the piezoelectric film replaces traditional separators between active electrodes. The efficiencies of conversion and storage in these rectification-free piezo-supercapacitor devices are better than those of other rectifier-based devices as the energy losses are less.^[41] In addition, this flexible and all-solid-state supercapacitor is an ideal energy storage device where the gel electrolyte is uniformly dispersed, as well as sandwiched in between two supercapacitor electrodes that also make the device leak-proof, unlike liquid-state supercapacitors. This also makes the device more suitable for energy generation and storage under mechanical pressure.^[38] Hence, the fabrication of a novel solid-state self-charging supercapacitor device, incorporating unique heterostructured electrode materials and a high-performance piezo-separator has the potential to achieve both superior energy storage as well as self-charging capabilities, making it highly beneficial for portable applications.

Herein, we have developed an all-solid-state, flexible, environmentally safe, fast charging self-powered asymmetric supercapacitor (SPASC) device using onion scale as the bio-piezoelectric energy harvester, as well as the separator in the device. For the first time, a Ni–Cu-MOF derived nickel-copper double hydroxide (NCDH) has been employed as the positive

and manganese dioxide decorated activated porous carbon (MnO_2 -APC) as the negative electrodes for excellent storage capacity along with poly(vinyl alcohol–potassium hydroxide) (PVA-KOH) electrolyte coated onion scale as bio-piezoelectric separator (BPS). The onion scale serves dual functions, as a separator of the supercapacitor and piezoelectric energy harvesting material that transforms mechanical energy into usable electrical energy. The distinctive and interesting aspect of this work lies in the dual functionality of the onion scale, representing a quite new finding worth highlighting. To the best of our knowledge, the use of three-dimensional porous NCDH obtained hydrothermally from Ni–Cu-MOF precursor serving as the positive electrode material with a high value of capacitance, which has not been previously documented in the literature. Here, for the first time, we have used Ni–Cu-MOF derived NCDH as the positive electrode material and onion scale as the BPS for the SPASC device. The final SPASC device demonstrates a specific capacitance (C_{sp}) value of ~165.77 F/g (at a current density of 1 A/g) spanning a broad potential window of 0–1.55 V. Moreover, the as-fabricated SPASC device demonstrates an impressive energy density of ~55.3 Wh/kg, coupled with exceptional electrochemical stability, retaining 91.5% of its initially obtained capacitance even after ~8000 charge-discharge cycles. Even, after 55 cycles under repetitive mechanical deformation, the device shows outstanding stability and durability. The self-charging capabilities of the SPASC device also exhibit remarkable performance, achieving a charge up to ~235.41 mV within 180 s without the need for a rectifier, indicating its promising potential as a self-powered energy storage device.

Experimental Section

Materials Details

Copper (II) chloride dihydrate [$\text{CuCl}_2 \cdot 2\text{H}_2\text{O}$], nickel (II) chloride hexahydrate [$\text{NiCl}_2 \cdot 6\text{H}_2\text{O}$], 2-methylimidazole [2 MIM], potassium permanganate [KMnO_4], manganese (II) chloride [MnCl_2] and methanol [CH_3OH] were obtained from Merck, Germany. Potassium hydroxide [KOH] flakes, polyvinyl alcohol [PVA], isopropyl alcohol and potassium carbonate [K_2CO_3] were purchased from Loba Chemie. Pvt. Ltd., India. All the analytical grade reagents are employed in this work without any chemical modification. Commercially available carbon-coated stainless steel (SS) fabric sheet was used as the flexible current collector. Biaxially oriented polypropylene (BOPP) tape and transparent polyethylene terephthalate (PET) film were bought from the local market. Onion skin and onion scale were collected from the local market. DI water used in this work was acquired from a JL-RO 100 Millipore-Q plus water purifier.

Synthesis of the Electrode Materials and Fabrication of the All-Solid-State Device

Step I: Synthesis of Porous NCDH (Positive Electrode Material)

The positive electrode material, NCDH was prepared by simple hydrolysis of Ni–Cu-MOF to get dense stacking and robust structure.

Synthesis of the Ni-Cu-MOF

Within a classical preparation process of Ni–Cu-MOF, 0.1 M $\text{CuCl}_2 \cdot 2\text{H}_2\text{O}$ and 0.4 M 2-methylimidazole (2MIM) were added in 20 mL methanol and stirred with a magnetic stirrer to get a homogeneous mixture and the solution was kept at 80 °C for 24 h. A 0.05 M solution of $\text{NiCl}_2 \cdot 6\text{H}_2\text{O}$ in 20 mL methanol was added to the residue and kept for another 24 h at 80 °C. After cooling the Ni–Cu-MOF was collected for hydrolysis.

Preparation of Porous NCDH

1 g of the Ni–Cu-MOF precursor was added to 30 mL 0.5 M KOH solution. The mixture was then transferred to a Teflon-lined hydrothermal and kept at 120 °C for 3 h. The resulting residue was then naturally cooled down to room temperature, followed by repeated washing with DI water followed by ethanol. Finally, the obtained product was dried at 60 °C for 12 h in a vacuum oven. The obtained NCDH as positive electrode material was then taken for electrochemical characterization and coated on a SS fabric sheet for device fabrication.

Step II: Preparation of MnO_2 -APC (Negative Electrode Material)

The negative electrode material, MnO_2 -APC was obtained from bio-waste onion skin by following the processes appended below.

Synthesis of the Activated Porous Carbon (APC)

Bio-waste onion skins collected from the local market were washed thoroughly with DI water and subsequently dried in air oven at 80 °C for 24 h. 10 g of that clean, dried onion skin were soaked in 100 mL of 2 M aqueous K_2CO_3 solution for 3 h. Then the residues were collected by filtering the solution and kept at 80 °C for 24 h. The dried residue was then heated in a tubular furnace for 1 h at 800 °C at a heating rate of 5 °C/min under argon flow. through this process carbonization as well as activation was achieved simultaneously. The carbonized sample was then neutralized with 1 M HCl, rinsed multiple times with DI water to ensure complete removal of any inorganic salts. The obtained solid was then dried overnight in a vacuum oven at 80 °C. The dried activated porous carbon was then collected to hydrothermally mix with MnO_2 .

Preparation of MnO_2 -APC

0.52 g of activated porous carbon was thoroughly dispersed in 30 mL DI water using ultra-sonication for 1 h. After that, 0.21 g of KMnO_4 and 0.31 g of MnCl_2 were added to that well-dispersed solution and stirred with a magnetic stirrer to get a homogeneous solution mixture. The total solution mixture was then transferred to a Teflon-lined hydrothermal and kept at 160 °C for 15 h. The resulting solid residue was then washed multiple times with both DI water and ethanol, followed by drying in a vacuum oven at 80 °C for 12 h. The obtained MnO_2 -APC was taken as negative electrode material for electrochemical characterizations and coated on a SS fabric sheet for device fabrication.

Step III: Fabrication of Bio-Piezoelectric Separator (BPS) Using Onion Scale

The onion scale (termed as BPS), peeled off from onion, was thoroughly washed with DI water and ethanol. Then after drying at room temperature for 24 h, the onion scale was cut into a

rectangular piece and soaked in PVA-KOH gel electrolyte to use as the separator in the device.

Step IV: Fabrication of All-Solid-State Self-Powered Asymmetric Supercapacitor (SPASC) Device

A flexible, all solid-state self-charging, asymmetric supercapacitor power cell was fabricated using NCDH coated SS sheet (NCDH@SS) as the positive electrode and MnO_2 -APC coated SS sheet (MnO_2 -APC@SS) as the negative electrode, where the onion scale, soaked in PVA-KOH gel (used as the electrolyte) served as the bio-piezoelectric separator in between the electrodes. Prior to assembling all the components, the gel electrolyte was also uniformly applied on the active surfaces of the electrodes. Subsequently, the electrodes coated with PVA-KOH electrolyte and the BPS were gently assembled together, followed by constant encapsulation with a BOPP tape to protect the device from damage during the application of mechanical forces as well as from the external environment. The schematic diagram for the fabrication of the SPASC device by assembling the electrodes and bio-separator is demonstrated in Figure 1.

2. Characterizations

The powder X-ray diffraction (PXRD) patterns of the materials were acquired by mounting the sample on PANalytical Empyrean diffractometer (PANalytical, Netherlands) with a monochromatic Cu K_α radiation ($\lambda = 0.15418 \text{ nm}$). X-ray photoelectron spectroscopic analysis (XPS) was achieved using PHI 5000 Versa Probe II type spectrometer (with Al K_α source $\sim 1486 \text{ eV}$). The survey scan of the materials was recorded with reference to aliphatic carbon (B. E. $\approx 283 \text{ eV}$). Morphology of the as-prepared materials was studied using a field emission scanning electron microscopic (FE-SEM) in Zeiss Merlin within an operating voltage of 5 kV, and transmission electron microscopic analysis (TEM, JEM-2100, JEOL, Japan). Quantitative elemental identification was made by using an energy dispersive X-ray spectrometer (EDS) connected with the FE-SEM. (NEXUS-870, Thermo Nicolet) was used to record fourier transform infrared spectrum (FTIR) within a range of $4000\text{--}400 \text{ cm}^{-1}$. The Raman spectroscopic analysis was executed with a Raman triple spectrometer (T-64000, HORIBA Jobin Yvon, France). Nitrogen adsorption isotherm was estimated at 77 K using a Quantachrome Quadrasorb-SI analyzer. Before performing the adsorption isotherm measurement, the samples were degassed at 100 °C for 12 h. The Brunauer–Emmett–Teller (BET) surface area was analyzed using the nonlocal density functional theory (NLDFT) method. Electrochemical analysis of the SPASC device was performed using a CHI-760 electrochemical workstation. In a three-electrode set-up, electroactive materials coated SS was used as the working electrode, while a platinum wire was used as the counter electrode and Ag/AgCl electrode as the reference electrode. The comprehensive electrochemical analysis of the SPASC device was performed using a conventional two-electrode cell set-up with NCDH@SS as the positive and MnO_2 -APC@SS as the negative electrodes, whereas, the BPS coated with PVA-KOH (gel electrolyte) used as the separator in between two electrodes. The output voltage of the nano-

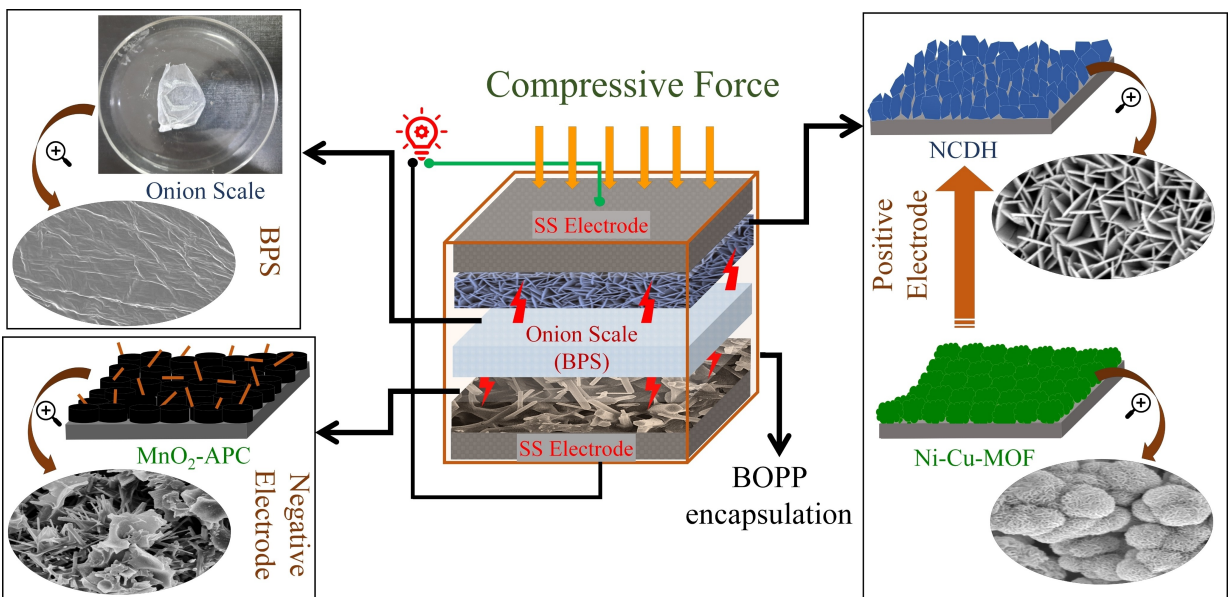


Figure 1. Schematic representation of as-prepared NCDH@SS sheet (right panel), MnO_2 -APC@SS sheet electrodes, and onion scale (left panel) encapsulation in BOPP tape for all-solid-state SPASC device (middle panel) fabrication.

generator (BPS) was estimated by using a digital oscilloscope (ROHDE & SCHWARZ, RTM-2022) having an input impedance of $1\ \text{M}\Omega$. The short circuit current of the nanogenerator was analyzed by an electrometer (Keithley-4220). The self-charging-discharging ability of the SPASC device was monitored by using the CHI-760 electrochemical workstation. A multimeter (FLUKE 115 true RMS) was used to monitor the generated output voltage during practical implementation.

3. Results and Discussion

3.1. Working Mechanism of the As-Prepared SPASC Device with Its Bio-Piezoelectric Separator

The pressure induced energy harvesting and storage mechanism of the as-fabricated SPASC device depends on the piezoelectric potential driven electrochemical reactions (oxidation and reduction) within the device (Figure 2). The SPASC device is assembled of four important parts that facilitate to harvest and storage of the energy altogether: MOF derived NCDH@SS sheet as the positive electrode, MnO_2 -APC@SS sheet as the negative electrode, PVA-KOH gel as electrolyte and an onion scale as the bio-piezoelectric separator. Here, the energy harvesting unit, onion scale is mainly composed of cellulose where different $-\text{OH}$ groups of the glucose from one chain form hydrogen ($-\text{H}$) bonds with oxygen atoms with the same or neighboring chain in the highly networked structure. The cellulose microfibrils within the crystal lattice spontaneously form electric dipoles due to the presence of $-\text{H}$ bonds that hold the chains together alongside very firmly. Therefore, the displacement or reorientation of the dipole in the crystal lattice produces piezoelectric potential in the cellulose on the application of an external force.^[42] In addition to providing

electricity for regular charging, the BPS also serves as a natural separator. The SPASC device is based on mainly two mechanisms involving two successive phenomena, which are: (i) piezoelectric potential generation at the BPS surface, and (ii) electrochemical processes propelled by the produced piezoelectric potential on the separator.^[38,43] At the initial stage, when there is no applied external force or mechanical deformation, the device is in discharged condition (Figure 2a). At this stage, no electrochemical reaction is there, as an electrochemical equilibrium between the electrodes and the gel-electrolyte is maintained. On application of external compressive stress on the top surface of the SPASC device by means of finger imparting, the BPS gets polarized due to the piezoelectric effect.^[44] A positive and a negative potential is created at the opposite surfaces of the BPS as a result of the potential difference formed across the width of the BPS, which drives the electrolytic ions (PVA-KOH) in the direction of the respective electrodes. The positive ions of the electrolyte i.e., K^+ ions move in the direction of the negative electrode and finally find their way onto the MnO_2 -APC surface, whereas the negative ions of the electrolyte (OH^- ions) migrate in the direction of the positive electrode and react with the positive electrode material, resulting the liberation of free electrons on the respective electrode. Thus, an electrochemical imbalance was induced within the electrolyte and both electrodes as a result of the ionic movement. To uphold the charge neutrality, the current collector substrate of the positive electrode gathers these free electrons and transfers them to the negative electrode. There are two pathways in which the electrons can be transported, either internally through the separator or through an external circuit via a monitoring system (electrochemical workstation). Upon application of continuous force on the device, more K^+ ions get inserted inside the negative electrode, which charges the device automatically. The gen-

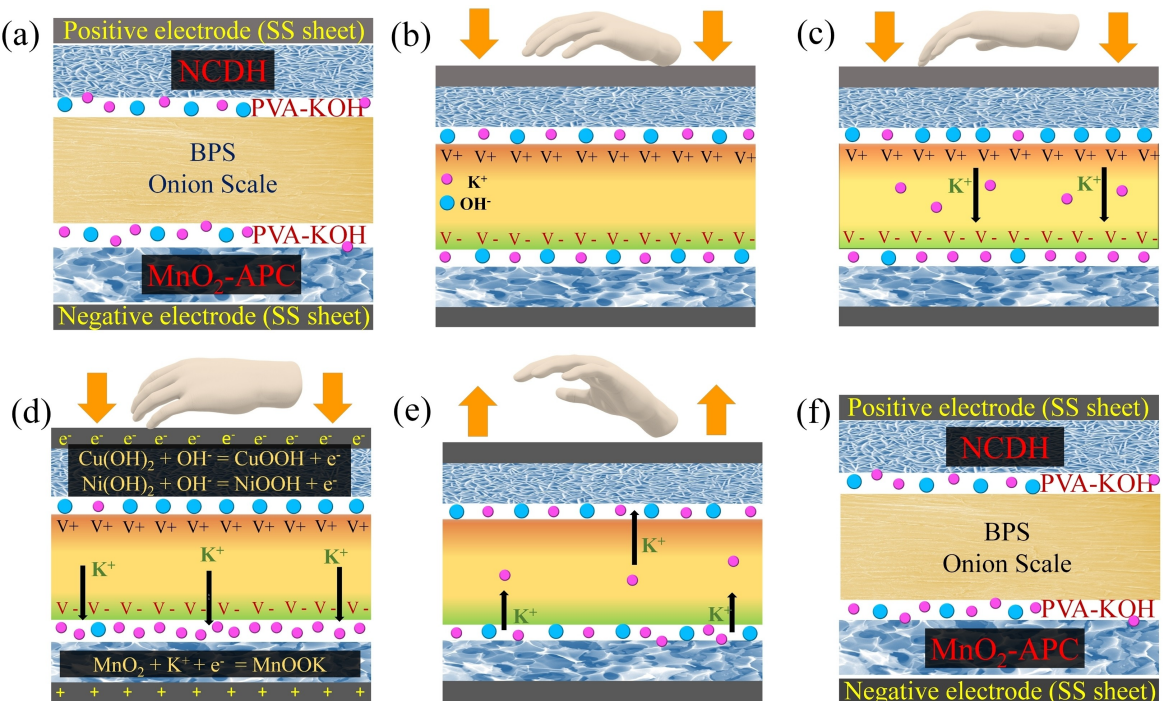


Figure 2. Schematic representation of the self-charging mechanism of the as-fabricated SPASC device under applied mechanical force. (a) Primary state of the device with no applied mechanical force, (b) generation of piezoelectric potential within the BPS under applied mechanical force, (c) generated piezoelectric potential driven movement of K^+ ions in direction of the negative electrode, (d) the corresponding electrochemical reactions occurring at the respective electrodes, (e) migration of K^+ ions towards the positive electrode under releasing applied mechanical force, and (f) final state of the SPASC device when applied force was removed.

erated piezoelectric potential across the BPS was balanced by the migration of the K^+ ions. The charging procedure was repeated under constant compressive force until an electrochemical equilibrium was achieved between the two electrodes and the produced piezoelectric potential. At this point, the device experiences no additional ionic polarization. The SPASC device directly converted the applied mechanical energy into electrochemical energy through the mentioned process. Besides, when the external mechanical force is removed, the piezoelectric potential across the BPS gradually disappeared, which breakdowns the electrochemical equilibrium of the SPASC device. To balance the equilibrium, a few K^+ ions slowly migrate back which discharges the device gently and complete the charging cycle (Figure 2e). Finally, a nominal inherent voltage is generated as some of the K^+ ions remain on the negative electrode even after discharging (Figure 2f). The Nernst equation, depicts the connection between electrode potentials and ion concentration, may also be used to describe the self-charging mechanism.^[45,46] The concentration of the K^+ ion slowly drops on the positive electrode side and moves towards the negative electrode end and concentrates there, on generation of the piezoelectric field by applying force. The counter part of the electrolyte, i.e., OH^- also varies the redox potential of both electrodes. Therefore, the electrolyte ion concentration gradient is created between the two electrodes, helping the SPASC device to self-charge. Additionally, the device was designed in such a way that the BPS and the electroactive materials remain in close proximity to one another

in order to use the piezoelectric field more effectively.^[37,46] The fundamental characteristics of both the electrode materials and the BPS are described below.

3.2. X-Ray Diffraction (XRD) Analysis

The structural characteristics of the electroactive materials were ascertained via XRD analysis. The XRD pattern of the as-prepared positive electrode material (NCDH) hydrolyzed from Ni–Cu-MOF is depicted in Figure 3a, where the absence of additional peaks at 21.03° , 26.59° , 37.22° , 41.78° , 70.13° , 93.26° in the XRD profile of NCDH, reveal the complete conversion of Ni–Cu-MOF to NCDH under the given reaction condition. Furthermore, the presence of the characteristic diffraction peak of $Ni(OH)_2$ and $Cu(OH)_2$ indicates the material is mixed-phase in nature. The 2θ peaks at 16.79° , 24.19° , 31.47° , 34.38° , 35.94° , 40.17° , 53.49° , 56.3° , and 64.95° can be referred as the (020), (021), (110), (002), (111), (130), (132), (023) and (152) planes respectively of the orthorhombic structure of $Cu(OH)_2$ [JCPDS# 13-420]. Whereas, the planes at 14.38° , 33.49° , 38.63° , 45.38° , 59.45° , 62.9° , 73.38° can be indexed to (001), (110), (101), (004), (111) and (201) planes of α and β form of $Ni(OH)_2$ [JCPDS# 38-0715 and JCPDS# 14-0117] indicating, the coexistence of both α and β $Ni(OH)_2$.^[47,49,50] The modest variation between acquired peak positions and the standard peak positions possibly due to the differences in the ionic radius of Cu and Ni ions.^[8,51] The obtained XRD pattern of the MnO_2 -APC and the

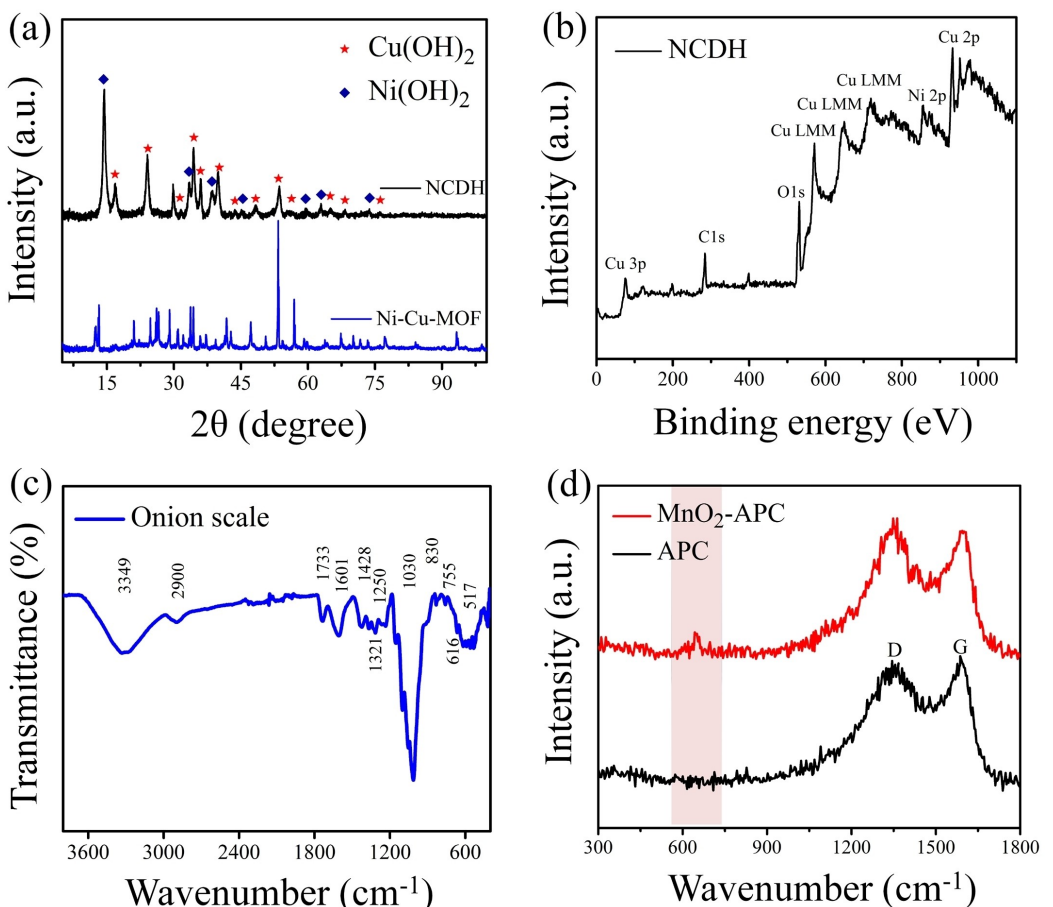


Figure 3. (a) XRD pattern of NCDH along with its precursor Ni–Cu-MOF. (b) XPS survey spectrum of NCDH. (c) FTIR spectrum of BPS. (d) Raman spectrum of activated porous carbon and MnO_2 -APC.

ion scale (BPS) has been demonstrated in Figure S1 in the supporting information (SI).

3.3. X-Ray Photoelectron Spectroscopic (XPS) Analysis

To determine the exact surface chemical composition and the chemical states of the component elements present in the NCDH and MnO_2 -APC, XPS study was performed. The complete XPS survey of NCDH, as shown in Figure 3b, suggests the coexistence of Ni 2p (854 eV), Cu 2p (933 eV) and O 1s (531 eV) in the as-prepared NCDH. The depth profile scans of all the elements are depicted separately in Figure S2 in SI with a selected area depth profile scan. All the XPS spectra are collected with respect to carbon with a binding energy of ≈ 283 eV. The spectra are fitted well using a Gaussian fitting method. In Ni 2p spectrum of NCDH (Figure S2b), two spin orbit doublets are present at a binding energy of 254.63 eV and 272.59 eV, with a binding energy separation of 17.96 eV which are denoted as Ni 2p_{3/2} and Ni 2p_{1/2}. Ni 2p_{3/2} peak can be deconvoluted into a pair of peaks by careful peak fitting, that are located at 854.21 eV and 855.47 eV and match with the binding energy of Ni^{2+} and Ni^{3+} .^[52] The binding energy difference between Ni 2p_{3/2} main peak and the satellite peak (≈ 860.61 eV)

is 5.99 eV. Additionally, another satellite peak (≈ 878.40 eV) appears at an energy gap of 5.72 eV from the Ni 2p_{1/2} main peak. All the mentioned signatures of Ni 2p clearly show the presence of Ni (II) oxidation state together with a trace amount of Ni (III) state in NCDH electrode material. Due to the surface oxidation reaction of Ni(OH)_2 in the presence of air, Ni^{3+} is found in the NCDH. As depicted in Figure S2c, the acquired 2p spectrum of Cu manifests two spin-orbit doublets, which represent Cu 2p_{3/2} and Cu 2p_{1/2}. The high resolution Cu 2p spectrum can be fitted into six peaks, the peaks placed at 931.87 eV and 952.75 eV correspond to Cu^+ (may be the presence of Cu(OH) or Cu_2O that are at very low amount), and the peaks located at 935.87 eV and 955.75 eV reveal the presence of Cu^{2+} (Cupric hydroxide). The open 3d⁹ shell or paramagnetic chemical state of Cu^{2+} is associated with the two shakeup satellite peaks at 965.12 eV and 944.87 eV.^[53,54] Furthermore, the Gaussian fitted O1s spectrum (Figure S2d) shows three closely spaced peaks at 530.22 eV(O_I), 531.64 eV(O_{II}) and 533.35 eV(O_{III}). The different chemical environment within the material is the origin behind the appearance of three different peaks in O 1s. The survey spectrum and detailed XPS analysis of the as-prepared MnO_2 -APC and BPS are explained in Figures S3 and S4, Section E in the SI.

3.4. Fourier Transform Infrared Spectroscopic Analysis (FTIR) Analysis

The FTIR spectrum of the onion scale in Figure 3c displays its complex structure with several absorption peaks.^[44,55] Appearance of a broad intense peak at 3347 cm^{-1} denotes the -OH stretching of the cellulose present in the onion scale fiber. The absorption peaks near 2900 cm^{-1} in the spectra represent the stretching vibration of C-H groups of cellulose. The presence of peaks at 1733 cm^{-1} and 1250 cm^{-1} represents the (C=O) stretching of the ester and aldehyde groups of hemicelluloses and lignin in the onion scale. The band at 1601 cm^{-1} corresponds to the presence of carboxylic groups and N-H bending. The CH_2 scissoring and the O-H bending vibration of cellulose in the onion scale were confirmed by the presence of peaks at 1428 cm^{-1} and 1321 cm^{-1} , respectively. The appearance of peaks at $\sim 1030\text{ cm}^{-1}$ and $\sim 896\text{ cm}^{-1}$ represent the C-O stretching and C-O-C deformation at glycosidic linkage of cellulose. The bands between $650\text{--}480\text{ cm}^{-1}$ in the spectra correspond to the stretching frequency of the N -containing oligoligands.^[56]

3.5. Raman Spectroscopic Analysis

The internal characteristic structural information of the APC and MnO_2 -APC can further be detected by Raman spectroscopy as

depicted in Figure 3d. The conventional two Raman active bands are clearly evident in the Raman spectrum of the APC at 1351.8 cm^{-1} (D band) and 1386.6 cm^{-1} (G band), where D band signifies the lattice disorder in sp^3 carbon and G band appears due to bond stretching of sp^2 carbon. The intensity ratio of the D band and G band (I_D/I_G) indicates the degree of graphitization and the high ratio value corresponds to small degree of graphitization. In this case, I_D/I_G ratio of APC and MnO_2 -APC are 0.96 and 1.02, respectively, suggesting the low degree of graphitization of MnO_2 -APC due to the presence of MnO_2 nanorods that increases the disorderness of the structure. The appearance of the peak at 646 cm^{-1} more profoundly confirms the presence of MnO_2 in the material.

3.6. Field Emission Scanning Electron Microscopic (FESEM) and Transmission Electron Microscopic (TEM) Analysis

The microstructure and morphological features of both the electrode materials were studied through FESEM and TEM analysis, as displayed in Figure 4. It can be demonstrated from Figure 4a and b that NCDH consists of interconnected uniform aligned nanosheets with an average thickness of 18 nm which provide a 3-dimensional interconnected-porous, hierarchical morphology in NCDH and the open pores are of 20 nm to 200 nm sizes. This morphology provides a smooth pathway for electrolyte ions as well as assists plenty of electrochemically

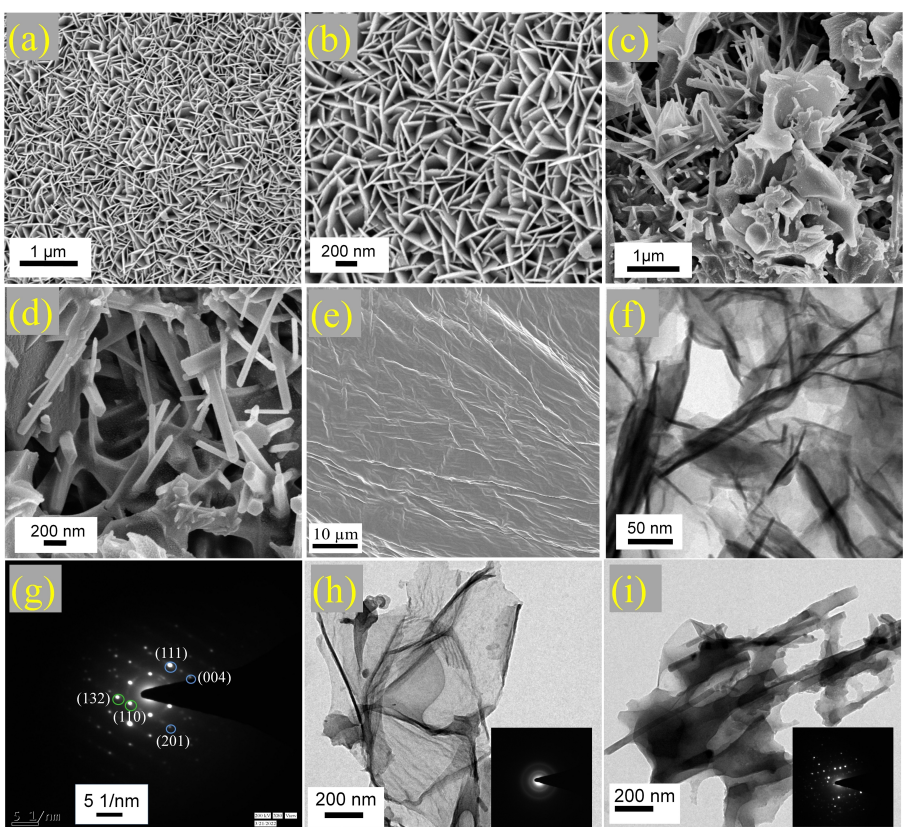


Figure 4. FESEM images of (a, b) porous hierarchical NCDH, and (c, d) MnO_2 -APC at different magnifications. (e) FESEM image of BPS. TEM images of (f) NCDH, (h) activated porous carbon, and (i) MnO_2 -APC. SAED patterns of (g) NCDH, (h inset) porous carbon, (i inset) MnO_2 -APC.

active sites for redox reactions which help to increase the capacitance (electrochemical properties) of the material. This 3-dimensional interconnected porous morphology of NCDH is developed from the flower-like morphology of Ni–Cu-MOF on hydrolysis, which provides enhanced porosity along with better stacking, as depicted in Figure S5 (SI). FESEM images of MnO₂-APC are displayed in Figure 4c and d, which clearly show the growth of MnO₂ nanorods (~540 nm) over the micrometer sized 3-dimensional open cavities of the activated porous carbon (Figure S7 in SI). These self-assembled, interconnected cavities on the surface of the APC are the result of K⁺ ion induced etching of the carbon framework at high temperature.^[57] The FESEM image of the BPS surface displayed in Figure 4e, shows a clear presence of well-aligned cellulose microfibrils, which suggests that under external forces it may exhibit piezoelectric property.^[44] The FESEM images of BPS at different magnifications is also shown in Figure S8 (SI). The TEM studies also express quite alike topographies to the FESEM analysis. The bulk morphological study of NCDH through TEM analysis is shown in Figure 4f, which confirms the presence of interconnected uniform thin nanosheets with a 3-dimensional porous morphology. The selected area electron diffraction (SAED) pattern demonstrates the crystalline nature of NCDH, as shown in Figure 4g.

The SAED pattern clearly indicates the prominent bright spots corresponding to the (110) and (132) crystal planes of Cu(OH)₂, as well as, additional bright spots representing (111) crystal planes along with less intense spots corresponding to (201) and (004) crystal planes of Ni(OH)₂. Figure 4h and i display the TEM images of 3-dimensional APC and MnO₂-APC, respectively, which show the presence of MnO₂ nanorod over the 3-dimensional interconnected porous assembly of APC. The SAED pattern clearly suggests the growth of the crystalline MnO₂ on the amorphous carbon by hydrothermal method. The selected area elemental mappings and energy dispersive X-ray line spectrum (EDS) of NCDH, as portrayed in the SI (Figure S6), demonstrate a balanced distribution of the constituent elements. From Figure S6(b–d), it is clearly observed that Ni, Cu and O co-exist in NCDH. Additionally, the co-existence of all these constituent elements was also confirmed by the EDS analysis (Figure S6e, SI). The morphological features of NCDH obtained after 8000 successive charge-discharge cycles (as demonstrated in Figure S13) support the eminent electrochemical stability of NCDH as the nanostructures remained almost intact after repeated operations.

3.7. BET Analysis

The porous nature and the effective exposed surface area of the electrode materials, NCDH and MnO₂-APC, were determined by the Brunauer-Emmett-Taylor (BET) analysis. Nitrogen adsorption-desorption isotherm of NCDH and activated porous carbon at 77 K shown in Figure S9 (SI). The adsorption isotherm (Figure S9a in SI) of NCDH follows a type III pattern along with H3 type hysteresis, suggesting that the loop essentially indicates the existence of predominant mesopores within the

electrode materials with a measured BET surface area of 100.5 m²/g. Using the nonlocal density functional theory (NLDFT) method, the pore size distribution of the mentioned electrode materials was calculated and the obtained pore width of the NCDH is 2.89 nm (Figure S9c in SI). The isotherm of the MnO₂-APC follows type IV adsorption isotherm (Figure S9b in SI). It shows a very high absorption at low relative pressure, indicating the presence of micropores, the small slope with a desorption hysteresis loop at the medium relative pressure denotes the development of the mesoporosity. The measured BET surface area of the MnO₂-APC is 692 m²/g and the obtained pore width (using NLDFT) is 1.17 nm (Figure S9d in SI). The high specific surface area of NCDH and the MnO₂-APC provide greater electrode-electrolyte interaction which enhances the overall electrochemical performance of the SPASC device.

3.8. Electrochemical Performances of Electrode Materials

All electrochemical characterizations, including cyclic voltammetry (CV), galvanostatic charge-discharge (GCD), electrochemical impedance spectroscopic (EIS) analysis, and cyclic stability of NCDH@SS and Ni–Cu-MOF@SS are described in SI (Section J.1), through a three-electrode cell setup in presence of 1 M KOH electrolyte. As can be seen, the NCDH@SS electrode exhibits a great electrochemical performance as well as cyclic stability (even after 8000 charge-discharge cycles at 1 A/g current density) within a working potential window of 0–0.55 V. To check the structural integrity of NCDH after the consecutive GCD cycles X-ray diffraction (XRD) analysis, Fourier transformed infrared (FTIR) spectroscopic study, X-ray photoelectron spectroscopy (XPS), Raman spectroscopy and morphological analysis through FESEM and TEM were conducted and comprehensively elaborated in Section H (SI). From the cooperative analysis, it is observed that NCDH@SS exhibits improved electrochemical properties than Ni–Cu-MOF@SS. Hence, it has been used as the effective positive electrode for the final SPASC device. Furthermore, the electrochemical characterization of MnO₂-APC@SS as the negative electrode of the SPASC device has been explained in SI (Section J.2). This analysis was carried out within a potential window of –1–0 V, in the presence of 1 M KOH (as the electrolyte) with a three-electrode cell arrangement. Before assembling the SPASC, the individual constituent positive and negative electrodes were separately analyzed through CV (at 3 mV/s scan rate) and GCD (at a current density of 1 A/g) to determine the working potential window of the final device. The CV and GCD profiles of the two component electrodes are collectively depicted in Figure 5 as a single diagram, which manifests that the working potential window of the SPASC device will be 0–1.55 V.

3.9. Electrochemical Performance of the All Aolid-State SPASC Device

To check the electrochemical performance of our fabricated device, CV, GCD, and EIS measurements were carried out within

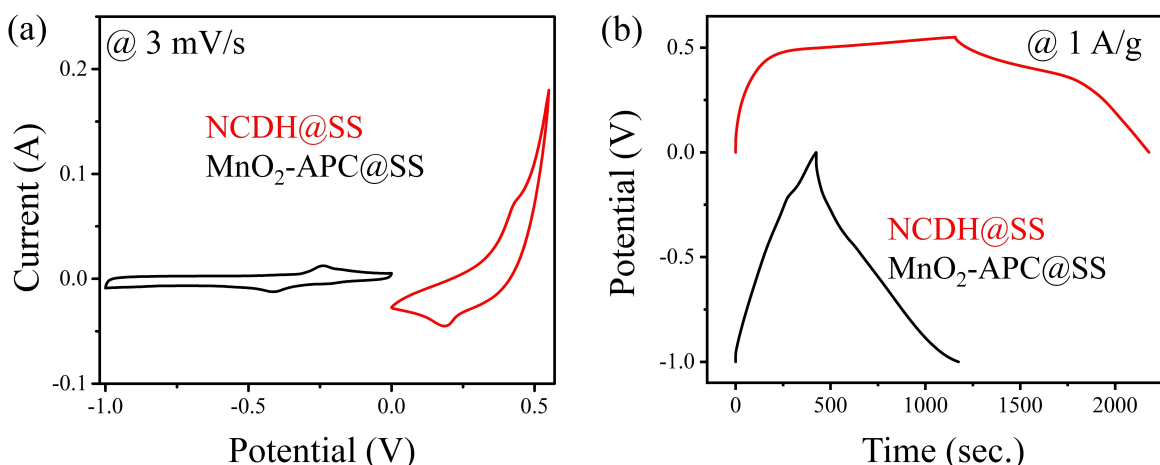


Figure 5. (a) CV profiles at 3 mV/s scan rate, and (b) GCD profiles at 1 A/g current density of NCDH@SS sheet (positive electrode) and MnO₂-APC@SS sheet (negative electrode).

the operating voltage window in the range of 0–1.55 V. The charge was balanced between the electrodes according to the equation $q^+ = q^-$, where q^+ represents the charge of the positive electrode and q^- represents the charge of the negative electrode, respectively. The stored charge and optimum mass ratio (m^+/m^-) of the positive and negative electroactive materials coated on the SS fabric sheet were calculated using Equations E3 and E4, provided in the SI. The maintained optimum mass ratio between the two respective electrodes was ~0.7. Before performing the electrochemical performance, the SPASC device was charged and discharged for 100 GCD cycles

at a 5 A/g current density to attain a steady capacitance value. The CV profiles of the SPASC device with varying scan rates within a working potential window of 0–1.55 V are illustrated in Figure 6a. Nature of the CV curves indicated the typical asymmetric behavior with the existence of both Faradaic and electric double layer capacitance by its distorted nature and redox peaks as a result of the presence of the two component electrodes. Excellent rate capacity of the SPASC device was indicated by all the CV curves, which showed nearly identical nature at all observed scan rates. The charging-discharging curves of our as-prepared device at various current densities are

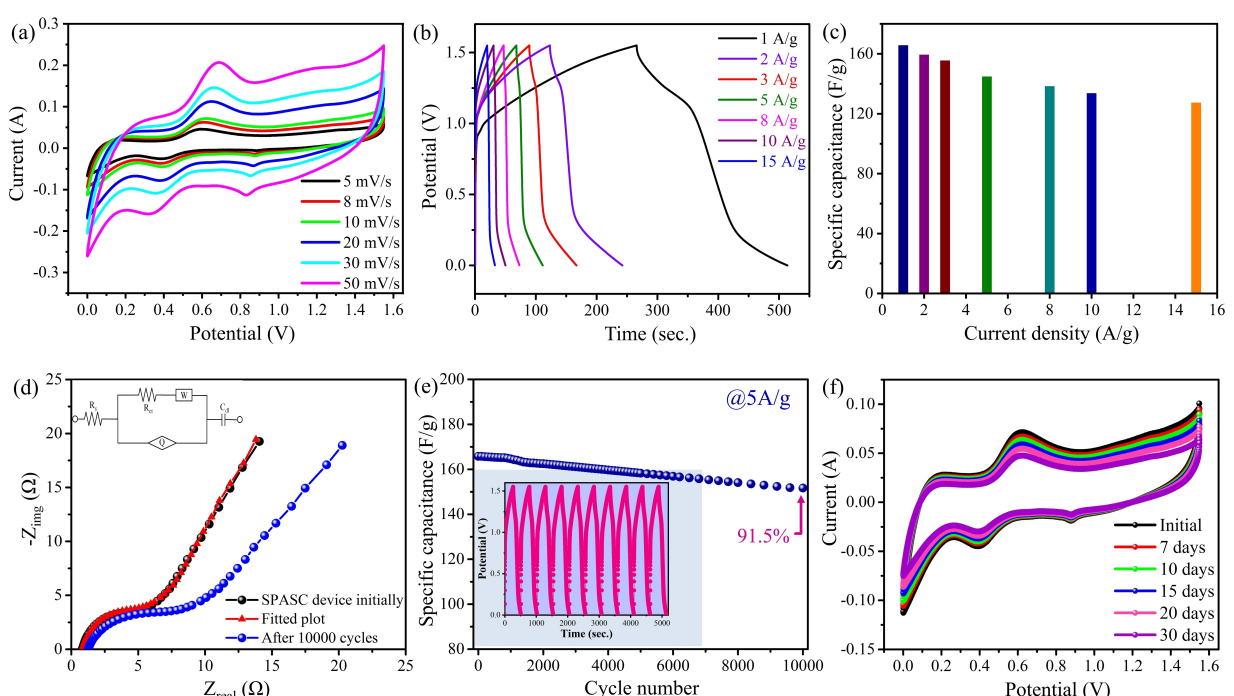


Figure 6. (a) CV plots at different scan rates, (b) GCD curves of the SPASC at various current densities, (c) variation of C_{sp} values with current density of the SPASC device. (d) Nyquist plot of the SPASC device at initial condition and after 10000 GCD cycles. (Inset depicts the equivalent fitted circuit diagram). (e) C_{sp} retention after 10000 consecutive GCD cycles at 5 A/g (The inset represents the 1st 10 consecutive GCD cycles at 5 A/g). (f) CV profiles of the SPASC device acquired after 7, 10, 15, 20 and 30 consecutive days from the device fabrication (Lifetime sustainability of the device).

shown in Figure 6b. At all the measured current densities, excellent capacitive performance of the SPASC device is revealed through the shape of its discharge profile with a plateau region. This plateau area developed as a result of several redox reactions that took place at the electrode/electrolyte contact, indicating that the faradaic capacitance has a significant contribution to the capacitance of the SPASC device. The obtained specific capacitance (C_{sp}) of the integrated SPASC device with the BPS was 165.77, 159.45, 155.55, 144.84, 138.34 and 133.71 F/g at a current density of 1, 2, 3, 5, 8 and 10 A/g respectively, (calculated using Equation E2, in SI) based on the total active mass of the electrode materials (1.95 mg). Even at a higher current density (15 A/g), the C_{sp} value maintains ~127.48 F/g, indicating significant electrochemical stability of the SPASC device. Remarkably, the calculated C_{sp} experiences a slow decrease up to 76.9% of its initial capacitance at a current density of 15 A/g and is illustrated in Figure 6c. This reveals superior electrochemical stability of the as-prepared SPASC device. The calculated energy density (E_{SPASC}) and the power density (P_{SPASC}) values (calculated using Equations E5 and E6 in SI) of the mentioned device at a current density of 1 A/g were 55.3 Wh/kg and 803.07 W/kg, respectively. The E_{SPASC} value of the device still maintains about 42.53 Wh/kg even at a considerably high P_{SPASC} value of 10936.2 W/kg (15 A/g). Table S1 (Section K, in SI) provides a concise comparison between the energy and power density of some previously reported asymmetric supercapacitor devices and the as-prepared SPASC device. The acquired EIS profile of the SPASC device initially and after 10000 consecutive GCD cycles appear quite similar in nature (Figure 6 d). A semi-circular arc in the higher frequency zone and a moderately steeper profile at the lower frequency zone were attained in the Nyquist plot of the SPASC device. However, the steeper nature of the EIS profile at low frequency region indicates that the electrolytes have more decent access to the electrode surface. In the inset of Figure 6d, the equivalent circuit fitted to the Nyquist plot is illustrated. The device exhibits a solution resistance (R_s) of 0.82 Ω and 1.23 Ω, while charge transfer resistance (R_{ct}) value of 5.49 Ω and 7.87 Ω at initial condition and after 10000 GCD cycles. Repeated cycling impacts the solution resistance (R_s) and charge transfer resistance (R_{ct}) due to the inefficient electrical contact between the electroactive materials and the SS sheet. The solution resistance is also affected by the sluggish ion transfer after consecutive cycles. As a result, the resistance value increased after 10000 cycles. The cyclic stability of the SPASC device was studied at a constant current density of 5 A/g through 10000 consecutive GCD cycles within a potential window of 0–1.55 V. Long-term cyclic stability was attained due to the stacked nanoflakes of NCDH by limiting the effective volume fluctuations throughout continuous cycling. The device notably retains about 91.5% of its initial C_{sp} value even after 10000 GCD cycles (Figure 6e). The inset of Figure 6e illustrates 10 consecutive cycles of the assembled device at a current density of 5 A/g. The sustainability of the SPASC device over its lifespan is illustrated in Figure 6f through cyclic voltammetry at 1 mV/s scan rate. Even after 30 days from device assembly, the nature of the CV plot remains nearly identical, while a slight reduction

in the area covered by the CV curves over the period suggests a promising lifespan for the device (Figure 6f). Additionally, the BOPP encapsulation also ensures excellent integrity among the electrodes, gel-electrolyte and the BPS as well as prevents the water evaporation from the gel electrolyte.^[37] All the collective results obtained from all the analyses can establish that our designed SPASC device is quite suitable member for flexible, portable, and all-solid-state electronic applications.

3.10. Energy Harvesting Performance of Onion Scale (BPS)

The piezoelectric performance of the BPS was tested separately using the fabricated piezoelectric nanogenerator (PENG) prior to assembling the SPASC device. The onion scale (1.5×1.5 cm²) was sandwiched between two SS sheets to assemble the PENG (mechanical energy harvester) for testing its piezoelectric properties, where SS sheet is used as the electrode. A piezoelectric potential was generated across the BPS upon continuous mechanical deformation. Figure 7a depicts that an average output voltage of ~18.21 V was attained by the PENG through frequent finger imparting with an applied force (F) of ≈16.25 N (f=3.8 Hz) (calculated using Equations E7 and E8 in SI). The current output of the PENG, under continuous finger imparting, is illustrated in Figure 7c. An average current of ~212 nA was achieved by the nanogenerator device (F≈16.25 N, f=3.8 Hz). Whereas, an output voltage of ~6.41 V was obtained, under repeated heel pressing with an applied force of ≈11.47 N (f=1.8 Hz), as demonstrated in Figure 7b. The output signal is quite stable even after 5000 cycles upon frequent finger imparting (F≈16.25 N, f=3.8 Hz) as illustrated in Figure 7d, suggesting excellent stability of the nanogenerator under mechanical deformation. This nanogenerator can maintain an average voltage of ~18 V even after 5000 times repeated finger imparting. To understand the stability cycles clearly first and last 25 s of the 5000 cycles are shown in Figures 7e and f, respectively. The mechanical stability and durability of the nanogenerator are further demonstrated with prolonged cyclic stability, as depicted in Figure S17 (SI). The stability of the BPS within the PENG device after 7 months is depicted in Figure S18 (SI). In the presence of –H bonds, the cellulose microfibril spontaneously forms electrical dipole without any electrical poling. Thus, it is evident that BPS is capable of generating piezoelectric potential in our fabricated SPASC device.

3.11. Self-Charging Performance of the as-Fabricated SPASC Device

The self-charging ability of our as-prepared SPASC device is illustrated in Figure 8 under mechanical deformation (compressive force). Figure 8a schematically represents the assembly of the all-solid-state flexible SPASC device in which BOPP tape is used to protect the device from any kind of external damage as well as to maintain the flexibility of the device. Thus, the applied mechanical force is more effective as compared to any device with traditional rigid stainless-steel cell, resulting in a

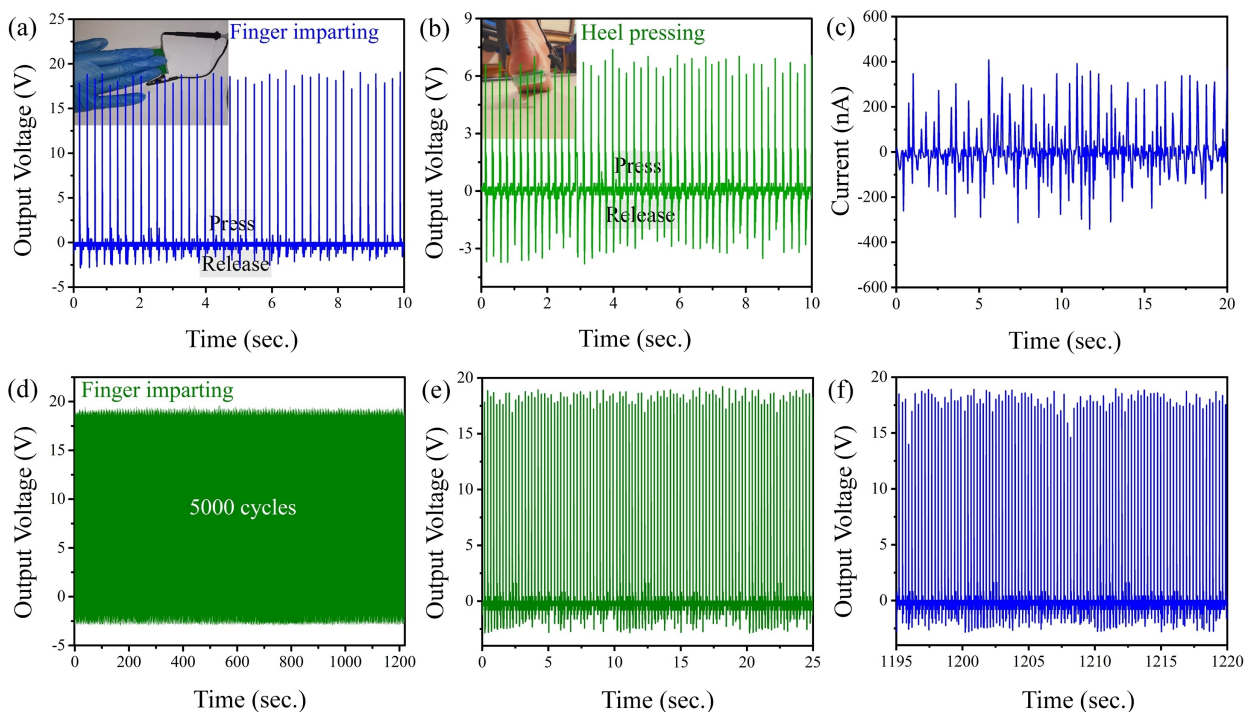


Figure 7. Output voltage produced by the BPS (a) under continuous finger imparting (the inset displays an image of finger imparting on the top surface of the BPS-based PENG), (b) upon frequent heel pressing (the inset illustrates an image of heel pressing on the PENG). (c) Short circuit current produced by the BPS under applied force. (d) Stability test of the BPS-based PENG through 5000 cycles, zoomed view of (e) first 25 s and (f) last 25 s of 5000 cycles.

higher piezoelectric voltage output. The higher piezoelectric voltage assists the movement of the electrolyte ions and improves the self-charging capability of the SPASC device. On application of 16.25 N force ($f=3.8$ Hz), the SPASC device was charged ~ 228.79 mV from the initial voltage of ~ 20.89 mV (charged 207.9 mV) within 123 s (Figure 8b). Following this, the SPASC device was then discharged to its primary voltage with a discharge current of $10\ \mu A$ over duration of about 127 s. The SPASC exhibits a storage capacity of about $0.220\ \mu Ah$. The possible explanation for the primary voltage (V_{oc}) of ~ 20.89 mV prior to charging is elucidated in SI (Section M). It has been noticed that the output voltage of the SPASC device varies with the frequency of the applied force, as depicted in Figure 8c. The device could be charged up to ~ 229.4 mV and ~ 204.17 mV, when the frequencies of the applied forces are 4 Hz and 2 Hz, respectively. A higher frequency leads to a better charging voltage because of the increased input power. Moreover, Figure 8d illustrates how the self-charging ability of the SPASC device is effected by the impact of applied force with a persistent frequency (4 Hz). The SPASC device exhibited output voltage up to 229.4, 220.19, 215.64 and 206.11 mV on application of 16.25, 12.5, 10.5 and 8.5 N forces, respectively. It has been observed that a significant applied force can enhance the output voltage, as the piezoelectric output amplifies with enhanced mechanical deformation. Figure 8e illustrates the cyclic self-charging and discharging performance of the SPASC upon an applied force of 16.25 N ($f=4$ Hz). Remarkably, the SPASC device displays very high stability even after undergoing 55 charging discharging cycles. This outcome also confirms the

mechanical and electrochemical longevity of the SPASC device. The enlarged view of the self-charging cycle is depicted in Section N (SI). As depicted in Figure 8f, the self-charging mechanism of the SPASC device directly correlates with the input of mechanical energy generated by the applied force. Under a compressive force of 16.25 N, the voltage of the SPASC device rises gradually up to ~ 235.41 mV from its initial voltage within 180 s. Whereas the voltage of the SPASC device remains relatively stable in the absence of the applied force. The device again experiences charging upon reapplication of compressive force. Table 1 provides a concise comparison of self-charging performances of some previously reported piezo-supercapacitor devices and our as-prepared SPASC device, indicating it as an excellent member of self-charging super capacitor group. With a continuous compressive force of 16.25 N through finger imparting, the SPASC device was gradually charged up to ~ 235.53 mV in 195 s, as illustrated in Figure S20 a (SI) and without any compressive force, the device got discharged almost near to its primary open circuit voltage (up to 27.43 V) in ~ 405 s. This indicates the holding capacity of the SPASC device after charging. Besides, the self-charging performance of the SPASC device in reverse connection (changing the polarity) is depicted in Figure S20b (SI). Under repeated mechanical deformations, the voltage of the SPASC device increased gradually from 30 mV to ~ 169.1 mV in the negative direction within 300 s and the device continued the stored charge for 150 s. This also confirms the self-charging behavior of the SPASC device. The power produced from repeated mechanical forces was used to drive several portable electronic devices and

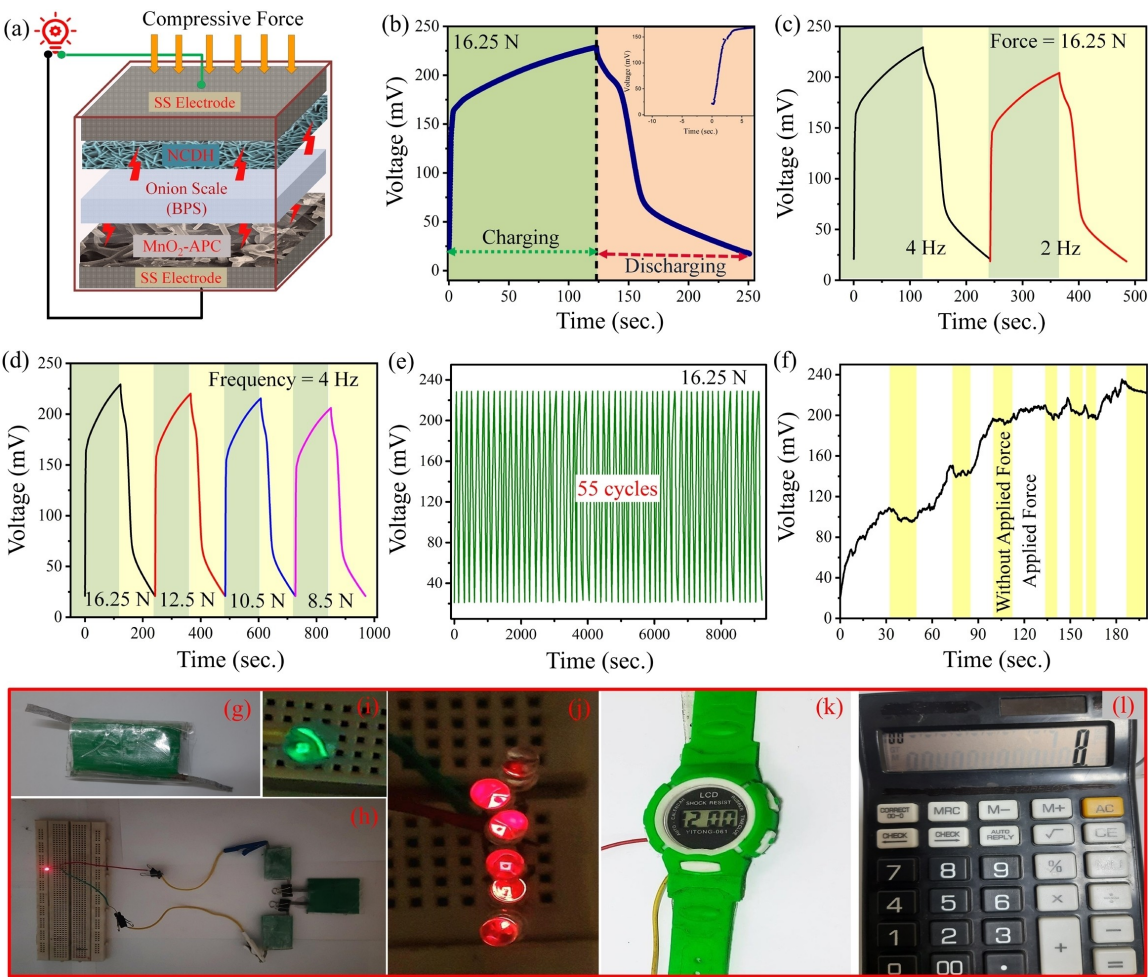


Figure 8. (a) Schematic illustration of the self-charging process of the SPASC device upon applied force. (b) The self-charging and discharging profile upon repeated finger imparting and the corresponding discharge process at constant-current (inset of b shows zoomed view of voltage change with time during charging). Self-charging behavior of the device (c) with different force frequencies, and (d) under different applied forces. (e) Stability of the device through self-charge-discharge cycles under constant compressive force. (f) The voltage of the SPASC device with and without applied force. The photograph of (g) the designed SPASC device and three serially connected SPASC devices as a sustainable power source to light up (h) one red LED, (i) one green LED light, (j) six commercial red LEDs. Photograph of powering-up (k) electronic wrist-watch, and (l) calculator by the SPASC device.

Table 1. Comparison of self-charging performances of our SPASC device with other reported results.

Electrode	Piezoelectric separator	Self-charging voltage (mV)	Ref.
Anode	Cathode		
Graphene	Graphene	PVDF film	112 (250 s)
Co-Fe ₂ O ₃ @ACC	Co-Fe ₂ O ₃ @ACC	PVA-KCl-BaTiO ₃	120 (420 s)
RGO@Cu foil	NiCoOH-Cuo@Cu foil	Fish Swim Bladder	151.2 (80 s)
Ni nanowires	Mg-Co nanowires	PVA-ZnO-KOH	55 (150 s)
NiCoP/NiCoN	Active carbon	P(VDF-TrFE)/BTO	132 (155 s)
MoS ₂ quantum sheets	MoS ₂ quantum sheets	Nafion solid polyelectrolyte	243 (420 s)
Activated carbon fabric	Activated carbon fabric	PAN	117.8 (300 s)
WS ₂ @PPy	WS ₂ @PPy	PVDF film	130 (60 s)
MnO ₂ -APC	NCDH	BPS (onion scale)	235.4 (180 s)
This work			

light-emitting diodes (LEDs). Upon frequent finger imparting, three serially attached SPASC devices (Figure 8h) are capable of providing sufficient power to lighten a green LED with sufficient

intensity (Figure 8i). Additionally, they are capable of concurrently lighting up six red LED lights (Figure 8j). Furthermore, these serially connected SPASC devices have the capability to

drive portable electronic wrist watch as well as a digital calculator (Figure 8k and l). The flexible nature of the SPASC device has been depicted by bending, twisting and rolling in Figure S21 (SI). From the above results, it can be resolved that our as-fabricated all solid-state flexible SPASC device can provide sufficient power to drive various smart portable electronics with its self-charging abilities. The compressive characteristics displayed by three SPASC devices connected in series during continuous finger imparting are demonstrated in the supporting videos (Videos S1 and S2). To demonstrate different types of tapping modes we applied forces to each device one by one.

4. Conclusions

In this work, we have demonstrated successful assembly of the superior electrode materials with onion scale as a bio-piezoelectric separator to fabricate an all solid-state self-powered asymmetric supercapacitor device. This as-fabricated SPASC device is composed of NCDH@SS sheet as the positive electrode and MnO₂-APC@SS sheet as the negative electrode using an onion scale (BPS) as the natural separator that acts as bio-piezoelectric nanogenerator as well. The bio-degradable, fluorine-free BPS undergoes self-polarization under mechanical deformation and generates an electric field, which leads the movement of electrolyte ions toward the electrodes. The distinct nanostructure of the electrode materials provides better electrode-electrolyte interaction, resulting superior stability and electrochemical performances. The SPASC device is efficient in harvesting electricity followed by storing as electrochemical energy. This flexible device exhibits decent cyclic stability under mechanical deformation within a large working potential window of 0–1.55 V. The SPASC device, with its rapid self-powering ability, can be effectively charged through two ways, either by applying electrical charging or through the application of mechanical and bio-mechanical (various body movements like hand pressing, elbow bending, knee bending, heel pressing, running etc) forces. A single rectification-free SPASC device is able to achieve a voltage up to ~235.41 mV from its primary open circuit voltage within 180 s through repeated finger imparting. The assembled SPASC device also simultaneously delivers excellent energy density (55.3 Wh/kg) along with a high power density (803.07 W/kg). Moreover, three SPASC devices connected in series powered up various portable electronic devices and LEDs under continuous mechanical force. Therefore, our as-fabricated flexible, stable and sustainable all solid-state SPASC device can provide new insight into the design and development of several flexible and portable next-generation integrated energy devices with self-charging abilities.

Author Contributions

P. Maity developed the concept and carried out the investigation, analysis, and manuscript writing. A. Maitra helped in

the analysis of results. S. Ojha, A. Mondal, A. Bera, S. Bera, and A. Das helped in the scientific discussion. B. B. Khatua helped with manuscript reviewing, defining the problems, and supervising the overall research work. All the authors have read and agreed to publish this manuscript.

Acknowledgements

This work was financially supported by The Department of Science and Technology (DST, Govt. of India) and Indian Institute of Technology Kharagpur. The authors gratefully acknowledge "DST-FIST for FESEM Facility at Materials Science Centre" and Materials Science Centre, IIT Kharagpur, for all other research facilities.

Conflict of Interests

The authors declare no competing financial interest.

Data Availability Statement

The data that support the findings of this study are available from the corresponding author upon reasonable request.

Keywords: SPASC • NCDH • Self-powered • Onion scale • Asymmetric supercapacitor

- [1] X. Shi, S. Chen, H. Zhang, J. Jiang, Z. Ma, S. Gong, *ACS Sustain. Chem. Eng.* **2019**, *7*, 18657–18666.
- [2] Z. L. Wang, *Adv. Funct. Mater.* **2008**, *18*, 3553–3567.
- [3] A. S. Aricò, P. Bruce, B. Scrosati, J.-M. Tarascon, W. van Schalkwijk, *Nat. Mater.* **2005**, *4*, 366–377.
- [4] Y. Hu, Y. Zhang, C. Xu, L. Lin, R. L. Snyder, Z. L. Wang, *Nano Lett.* **2011**, *11*, 2572–2577.
- [5] J.-H. Lee, J. Kim, T. Y. Kim, M. S. Al Hossain, S.-W. Kim, J. H. Kim, *J. Mater. Chem. A* **2016**, *4*, 7983–7999.
- [6] B. Luo, D. Ye, L. Wang, *Adv. Sci.* **2017**, *4*, 1700104.
- [7] M. Mahmood, A. Rasheed, I. Ayman, T. Rasheed, S. Munir, S. Ajmal, P. O. Agboola, M. F. Warsi, M. Shahid, *Energy Fuels* **2021**, *35*, 3469–3478.
- [8] A. Maitra, A. K. Das, R. Bera, S. K. Karan, S. Paria, S. K. Si, B. B. Khatua, *ACS Appl. Mater. Interfaces* **2017**, *9*, 5947–5958.
- [9] S. Ojha, P. Maity, S. Bera, S. Kumar Si, B. Bhusan Khatua, *Energy Technol.* **2023**, *11*, 2300157.
- [10] J. Yoo, S. Cho, W. Kim, J.-Y. Kwon, H. Kim, S. Kim, Y.-S. Chang, C.-W. Kim, D. Choi, *Nanotechnology* **2015**, *26*, 275402.
- [11] Y. Hu, Z. L. Wang, *Nano Energy* **2015**, *14*, 3–14.
- [12] S. K. Karan, R. Bera, S. Paria, A. K. Das, S. Maiti, A. Maitra, B. B. Khatua, *Adv. Energy Mater.* **2016**, *6*, 1601016.
- [13] S. Ojha, S. Paria, S. K. Karan, S. K. Si, A. Maitra, A. K. Das, L. Halder, A. Bera, A. De, B. B. Khatua, *Nanoscale* **2019**, *11*, 22989–22999.
- [14] A. Navid, C. S. Lynch, L. Pilon, *Smart Mater. Struct.* **2010**, *19*, 055006.
- [15] S. Khalifeh, in *Polymers in Organic Electronics* (Ed.: S. Khalifeh), ebook, ChemTec Publishing, **2020**, 341–391.
- [16] S. K. Ghosh, T. K. Sinha, B. Mahanty, D. Mandal, *Energy Technol.* **2015**, *3*, 1190–1197.
- [17] K. Krishnamoorthy, P. Pazhamalai, V. K. Mariappan, S. S. Nardekar, S. Sahoo, S.-J. Kim, *Nat. Commun.* **2020**, *11*, 2351.
- [18] P. Simon, Y. Gogotsi, *Nat. Mater.* **2020**, *19*, 1151–1163.
- [19] W. Tian, P. Ren, X. Hou, R. Xue, Z. Chen, Z. Guo, Y. Jin, F. Ren, *Int. J. Biol. Macromol.* **2024**, *261*, 129977.

- [20] Z. Fan, J. Yan, T. Wei, L. Zhi, G. Ning, T. Li, F. Wei, *Adv. Funct. Mater.* **2011**, *21*, 2366–2375.
- [21] Z. Zhai, L. Zhang, T. Du, B. Ren, Y. Xu, S. Wang, J. Miao, Z. Liu, *Mater. Des.* **2022**, *221*, 111017.
- [22] L. L. Zhang, X. S. Zhao, *Chem. Soc. Rev.* **2009**, *38*, 2520–2531.
- [23] Q. Wang, L. Zhu, L. Sun, Y. Liu, L. Jiao, *J. Mater. Chem. A* **2015**, *3*, 982–985.
- [24] S. A. Delbari, L. S. Ghadimi, R. Hadi, S. Farhoudian, M. Nedaei, A. Babapoor, A. Sabahi Namini, Q. V. Le, M. Shokouhimehr, M. Shahedi Asl, M. Mohammadi, *J. Alloys Compd.* **2021**, *857*, 158281.
- [25] M. Guan, Q. Wang, X. Zhang, J. Bao, X. Gong, Y. Liu, *Front. Chem.* **2020**, *8*, 390.
- [26] Q. T. Nguyen, U. T. Nakate, J. Chen, D. T. Tran, S. Park, *Compos. Part B Eng.* **2023**, *252*, 110528.
- [27] D. K. Yadav, J. Muhammed, S. Deka, *ACS Appl. Nano Mater.* **2023**, *6*, 13513–13523.
- [28] Z. Ali, M. Z. Iqbal, H. H. Hegazy, *J. Energy Storage* **2023**, *73*, 108857.
- [29] M. Alzaid, R. Alanazi, I. H. Alsohaimi, W. S. Mohamed, N. M. A. Hadia, M. Ezzeldien, M. Z. Iqbal, *Diam. Relat. Mater.* **2023**, *134*, 109737.
- [30] Q. Liao, N. Li, S. Jin, G. Yang, C. Wang, *ACS Nano* **2015**, *9*, 5310–5317.
- [31] C. Lu, X. Chen, *Acc. Chem. Res.* **2020**, *53*, 1468–1477.
- [32] J. Huang, K. Yuan, Y. Chen, *Adv. Funct. Mater.* **2022**, *32*, 2108107.
- [33] S. Vijaya, P. Sharma, B. Aljafari, S. Anandan, *Int. J. Energy Res.* **2022**, *46*, 23871–23878.
- [34] S. Wang, Z.-H. Lin, S. Niu, L. Lin, Y. Xie, K. C. Pradel, Z. L. Wang, *ACS Nano* **2013**, *7*, 11263–11271.
- [35] R. Song, H. Jin, X. Li, L. Fei, Y. Zhao, H. Huang, H. Lai-Wa Chan, Y. Wang, Y. Chai, *J. Mater. Chem. A* **2015**, *3*, 14963–14970.
- [36] S. Mondal, S. Thakur, S. Maiti, S. Bhattacharjee, K. K. Chattopadhyay, *ACS Appl. Mater. Interfaces* **2023**, *15*, 8446–8461.
- [37] A. Maitra, S. K. Karan, S. Paria, A. K. Das, R. Bera, L. Halder, S. K. Si, A. Bera, B. B. Khatua, *Nano Energy* **2017**, *40*, 633–645.
- [38] A. Ramadoss, B. Saravanakumar, S. W. Lee, Y.-S. Kim, S. J. Kim, Z. L. Wang, *ACS Nano* **2015**, *9*, 4337–4345.
- [39] C. Zhao, J. Xu, J. Tao, C. Xiao, X. Jin, W. Wang, X. Liu, J. Chen, Z. Zhu, *Nano Energy* **2023**, *116*, 108812.
- [40] X. Gao, Y. Zhang, Y. Zhao, S. Yin, J. Gui, C. Sun, S. Guo, *Nano Energy* **2022**, *91*, 106701.
- [41] S. Verma, S. Arya, V. Gupta, A. Khosla, *Chem. Eng. J.* **2021**, *424*, 130567.
- [42] E. Fukada, *Wood Sci. Technol.* **1968**, *2*, 299–307.
- [43] X. Xue, P. Deng, B. He, Y. Nie, L. Xing, Y. Zhang, Z. L. Wang, *Adv. Energy Mater.* **2014**, *4*, 1301329.
- [44] S. Maiti, S. Kumar Karan, J. Lee, A. Kumar Mishra, B. Bhusan Khatua, J. Kon Kim, *Nano Energy* **2017**, *42*, 282–293.
- [45] X. Xue, S. Wang, W. Guo, Y. Zhang, Z. L. Wang, *Nano Lett.* **2012**, *12*, 5048–5054.
- [46] X. Xue, P. Deng, S. Yuan, Y. Nie, B. He, L. Xing, Y. Zhang, *Energy Environ. Sci.* **2013**, *6*, 2615–2620.
- [47] L. Ping, G. Minarik, H. Gao, J. Cao, T. Li, H. Kitadai, X. Ling, *Spin-state Directed Synthesis of >20 micrometers 2D Layered Transition Metal Hydroxides via Edge-on Condensation* **2022**.
- [48] V. Kovaleko, V. J. B.-E. Kotok, *Eur. J. Enterp. Technol.* **2017**, *4*, 1722.
- [49] D. S. Hall, D. J. Lockwood, C. Bock, B. R. MacDougall, *Proc. R. Soc. A.* **2015**, *471*, 20140792.
- [50] X. Chen, X. Zhong, B. Yuan, S. Li, Y. Gu, Q. Zhang, G. Zhuang, X. Li, S. Deng, J. G. Wang, *Green Chem.* **2019**, *21*, 578–588.
- [51] J. Wang, Q. Zhang, X. Li, D. Xu, Z. Wang, H. Guo, K. Zhang, *Nano Energy* **2014**, *6*, 19–26.
- [52] D. Xiong, W. Li, L. Liu, *Chem. Asian J.* **2017**, *12*, 543–551.
- [53] H. Sun, O. A. Zelekew, X. Chen, Y. Guo, D.-H. Kuo, Q. Lu, J. Lin, *RSC Adv.* **2019**, *9*, 31828–31839.
- [54] J. Yu, J. Ran, *Energy Environ. Sci.* **2011**, *4*, 1364–1371.
- [55] J.-W. Rhim, J. P. Reddy, X. Luo, *Cellulose* **2015**, *22*, 407–420.
- [56] A. Chowdhury, A. Bhowal, S. J. W. Datta, *Water* **2012**, *4*, 37–51.
- [57] J. Wang, S. Kaskel, *J. Mater. Chem.* **2012**, *22*, 23710–23725.
- [58] S. Sahoo, K. Krishnamoorthy, P. Pazhamalai, V. K. Mariappan, S. Manoharan, S.-J. Kim, *J. Mater. Chem. A* **2019**, *7*, 21693–21703.
- [59] D. Zhou, F. Wang, J. Yang, L.-Z. Fan, *Chem. Eng. J.* **2021**, *406*, 126825.
- [60] S. Verma, P. Mahajan, B. Padha, A. Ahmed, S. Arya, *Electrochim. Acta* **2023**, *465*, 142933.
- [61] A. A. Kulkarni, N. K. Gaikwad, A. P. Salunkhe, R. M. Dahotre, T. S. Bhat, P. S. Patil, *J. Energy Storage* **2023**, *65*, 107362.
- [62] A. De Adhikari, S. Singh, I. Lahiri, *J. Alloys Compd.* **2023**, *939*, 168713.

Manuscript received: June 7, 2024

Revised manuscript received: August 19, 2024

Accepted manuscript online: September 10, 2024

Version of record online: October 29, 2024